Materials & Design 233 (2023) 112200

Contents lists available at ScienceDirect

Materials & Design

journal homepage: www.elsevier.com/locate/matdes

Elastic and plastic mechanical properties of lithium measured by nanoindentation

Ed Darnbrough *, Jack Aspinall, Mauro Pasta, David E.J. Armstrong

Department of Materials, University of Oxford, Parks Road, Oxford, OX1 3PH, United Kingdom

ARTICLE INFO

Keywords:
Lithium metal
Mechanical properties
Nanoindentation

ABSTRACT

Metallic lithium is the desired anode material for high energy density solid state batteries and shows a factor of four range in elastic modulus and two orders of magnitude difference in creep properties dependent on sample preparation and testing method. In this paper we use *in-situ* nanoindentation to measure the anisotropic mechanical properties from the BCC crystal structure and the effect of strain-rate and temperature, which have an impact on battery cycle performance. This work clarifies the reasons for the range of property values reported in the literature with a global equation for yield strength with strain-rate. From this information conclusions can be drawn around variables to optimise in order to minimise the required pressure for a chosen stripping critical current in solid state batteries.

1. Introduction

Lithium anodes theoretically give the highest capacity with the lowest density of all current candidate materials [1]. Dendrite and void formation during cycling have hindered the application of lithium in high energy density batteries [1,2]. It has been suggested that this is due to the mechanical behaviour of lithium given the experimental link between these failure mechanisms and the applied stack pressure, which has lead to a renewed interest in characterising the alkali metal [3–8]. The anisotropy in the elastic properties of the BCC metal has been reported in the late 1960s and more recently illustrated by Xu et al. [9–11]. There has been several attempts to characterise the yield stress and time dependent creep behaviour that has resulted in a reported two orders of magnetude range in the stress required to achieve a strain-rate of 0.01 s^{-1} [12–14]. Sedlatschek et al. used tensile measurements to demonstrate that lithium plasticity is rate dependent and LePage et al. used temperature to produce values for power-law creep in lithium including a number for the energy activation of dislocation climb [15,16]. However, Fincher et al. have observables different strain-rate dependencies with tensile tests and nanoindentation of lithium metal, with the later showing high hardness values at low depths [12]. Narayan and Anand tried to model the elastic-viscoplastic response of nanoindentation data from Wang et al. [17,14] on a larger scale showing that the stress required for a chosen strain-rate would increase with total strain and proposed significantly higher stress than observed in the macro-scale experiments. The lithium creep properties and yield strength have been shown by the work by Masias et al. to be different for compression and tensile experiments on the same sample scale [13,18]. Raj has highlighted the importance of fully understanding the creep behaviour of lithium for solid state batteries by suggesting a linear relationship based on dislocation motion between stack pressure and current density that delineates when batteries will fail [19].

All recent solid state battery advances are using lithium metal anodes at small-scales where the mechanics are important for understanding plating and stripping [20]. The importance of the creep properties and ductility of lithium metal has been highlighted by being beneficial for void formation but detrimental for dendrite formation [21,22]. The lithium metal mechanical properties also have some importance for Li-ion systems where metal is platted during cycling as the incompressibility of nanoscale platted lithium can lead to irreversible cell thickness increases [23].

Here we investigate metallic lithium using nanoindentation testing to deconvolute the effects of experimental methods and sample preparation that have led to a range of elastic modulus, yield strength, and creep results in the literature.

Lithium is soft and exhibits a time dependent mechanical behaviour that is characterised as visco-elastic if it is recoverable and visco-plastic if non-recoverable [14,24,25]. The two types of deformation have been difficult to convolute using standard nanoindentation, requiring oscillating tests like dynamic mechanical analysis (DMA) where the time

* Corresponding author.
E-mail address: ed.darnbrough@materials.ox.ac.uk (E. Darnbrough).

https://doi.org/10.1016/j.matdes.2023.112200
Received 30 March 2023; Received in revised form 19 July 2023; Accepted 28 July 2023
Available online 4 August 2023

period of recovery can be monitored [14,26]. Visco-plastic behaviour is described as plastic strain accumulated from a stress above the yield point or by conversion from elastic strain during stress relaxation [27]. Previous attempts have been made to model the visco-plastic of lithium in specific cases as an incompressible viscous fluid [8] or with the Perzyna viscoplasticity model [28] that focus on low stresses or high tensile loads, respectively. We consider if a metal is yielding the strain-rate is heavily dependent on the dislocation density as shown by the Orowan equation (equation (1)) that can be understood as the net movement of dislocations at an average velocity giving rise to plasticity [29]. The simplest description of the average dislocation velocity (v_{av}) with applied stress (τ) is to assume a linear drag coefficient (B) meaning that $v_{av} = b\tau_O/B$. Where B has units of Pa.s and is on the order of 1×10^{-5} in most transition metals [30]. This gives the stress from this mechanism as equation (2). Typically yield strength of a material is related to Taylor hardening due to the dislocation density, equation (3). As shown by Nix and Gao, and discussed below, this approach can be applied in nanoindentation using equation (4) [31]. This then gives the total stress required to yield a material (τ_{app}) can be considered from the Taylor equation and the additional stress above that is responsible for the speed of deformation or strain-rate as a rearrangement of the Orowan equation, equation (5) [29].

$$\dot{\epsilon}_p = m f_a \rho_y b v_{av} \tag{1}$$

$$\tau_O = \dot{\epsilon}_p B / m f_a \rho_y b^2 \tag{2}$$

$$\tau_T = \alpha G b \sqrt{\rho_y} \tag{3}$$

$$where \quad \rho_y = \frac{3tan^2\theta}{2bh} + \rho_s \tag{4}$$

$$\tau_{app} = \tau_O + \tau_T \tag{5}$$

where m is the Schmitd factor; f_a is the fraction of mobile dislocations that are on active slip planes; ρ_y is the dislocation density at yield; ρ_s is the statistically stored dislocation density of the material; b is the Burgers vector; G is the shear modulus; h is the indentation depth; α a geometric constant of 0.5 and θ is the angle between the surface of the indenter tip and the plane of the material surface making $tan\theta = 0.385$ for the Berkovichi tip geometry [31]. It can be seen from this equation that where the dislocation density is high the stress is dominated by Talyor hardening and when low it is dominated by the strain-rate. Further discussion of the other implications from this combination of effects can be found the in the paper by Fan et al. 2021 [29].

Nix and Gao showed that nanoindentation hardness at small depths is dominated by strain gradient effects due to a high dislocation density generated by the geometry of the sharp tips [31]. Their work suggests that the geometrically necessary dislocations caused by the tip at low depth can be used to calculate a relationship for the dislocation density with depth. The work of Nix and Gao showed this for a material with no viscosity; as the nanoindentation hardness of a material is greatest at low depths and decreases as those depths increase that is illustrated by the change in dislocation density. Some work has observed the nanoindentation strain-rate sensitivity in BCC metals and lithium [32,12]; however, here we will focus on the role of strain-rate with dislocation density to give a full picture of lithium as a material. This interpretation of the dislocation density calculated from the tip depth (equation (4)) during a test can then be combined with equation (5) to deconvolute the strain hardening and dislocation hardening plastic behaviour of the material.

2. Methods

Lithium sample surfaces are prepared by cutting off any contamination to produce a fresh surface of a foil (0.75 x 5 x 5 mm, purity 99.9% purchased from Sigma Aldrich) using a microtome blade in an Ar atmosphere immediately prior to placing in the scanning electron microscope (SEM). Samples are mounted so that they can easily be rotated between positions for electron backscatter detection (EBSD) and nanoindentation, further information on this procedure can be seen in reference [33]. This is all conducted without the sample coming into contact with air as the SEM chamber opens into the Ar glovebox where the samples are prepared.

Surface preparation for the study of lithium metal is very important given the easy formation of reaction layers with small amounts of oxygen or CO_2 [34,35]. It has been shown that EBSD pattern quality from lithium metal is particularly sensitive to low energy electrons that are easily absorbed by impurities or oxide layers. This implies that the ability to collect high quality EBSD patterns over a multi-millimetre length scale (Fig. 1a) is indicative of good surface preparation with minimal impurities that will not affect the measurements made by nanoindentation [33].

Nanoindentation tests are conducted with a PI88 Hysitron in a Tescan Mira 3 using load or displacement control. Typical tests use a linearly increasing load with a tip oscillation frequency of 100 Hz to measure hardness and elastic modulus with depth using a Berkovich tip shape that has been calibrated using fused silica [36]. This method is known as continuous stiffness measurement and uses the contact area and stiffness to give storage modulus values with depth that can be converted to Young's modulus, as shown in equation (6) [37]. A frequency of 100 Hz is chosen to maximise depth resolution while avoiding resonant effects that occur at higher frequencies that will be discussed in the visco-elastic section of this work. A mean modulus vs depth data set is calculated for each grain by combining all the tests in each grain (n>3) and a single mean average value with an associated standard deviation error is taken from the of values beyond 200 nm to avoid any issues of surface roughness.

$$E = \frac{\sqrt{\pi}}{2}\frac{S}{\sqrt{A_c}} \tag{6}$$

where S (Pa.m^{-1}) and A_c (m^2) are the measured stiffness and contact area, respectively. Visco-elastic properties are determined using nanoindentation dynamic mechanical analysis (nanoDMA) by considering the indenter and the sample as damped springs in series and measuring their response with a driven frequency. Here the dynamic compliance is measured and then normalised using the driving force to give a measure of the amplitude gain. The relationship with frequency is a simple combination of two coupled simple harmonic oscillators, the full mathematic steps are shown in the associated paper on ArXiv [38]. This method results in the measurement of a stiffness, k, and damping coefficient, d, which can be converted into Elastic modulus, E, and coefficient of viscosity, ν, given the depth at which the nanoindentation test is conducted. The elastic relaxation time is then $\frac{\nu}{E}$.

Visco-plastic properties can be measured using indentation stress relaxation and creep tests. Throughout the relationship between shear stress τ and hardness is assumed to be: $H = 3\sigma = 3\sqrt{3}\tau$. Indentation stress relaxation tests were conducted in displacement control and creep tests are conducted in load control. Creep tests are held at a load and the depth monitored with the fitting conduced by initially segmenting the data to consider the low strain-rate region alone and with the Orowan contribution as zero before using these fitting parameters as the initial input for an iterative minimisation of residual squares fitting of the test data as a whole. Elevated temperature tests were conducted with the same PI88 Hysitron in a Tescan Mira 3 instrumental set up with a heater attached to both the tip and the sample stage. The temperature of the two heaters was matched within 0.1 °C as monitored by embedded thermocouples. The total drift (thermal and instrumental) was monitored prior to each test and was consistently lower than 1 nm/s. The weight of the additional heater on the tip restricted the use of the vibration module used in room temperature tests and so partial unload test were conducted where the indenter holds at a load before unloading 90% and then reloading to a higher value, with this loop repeated for ten or more increments.

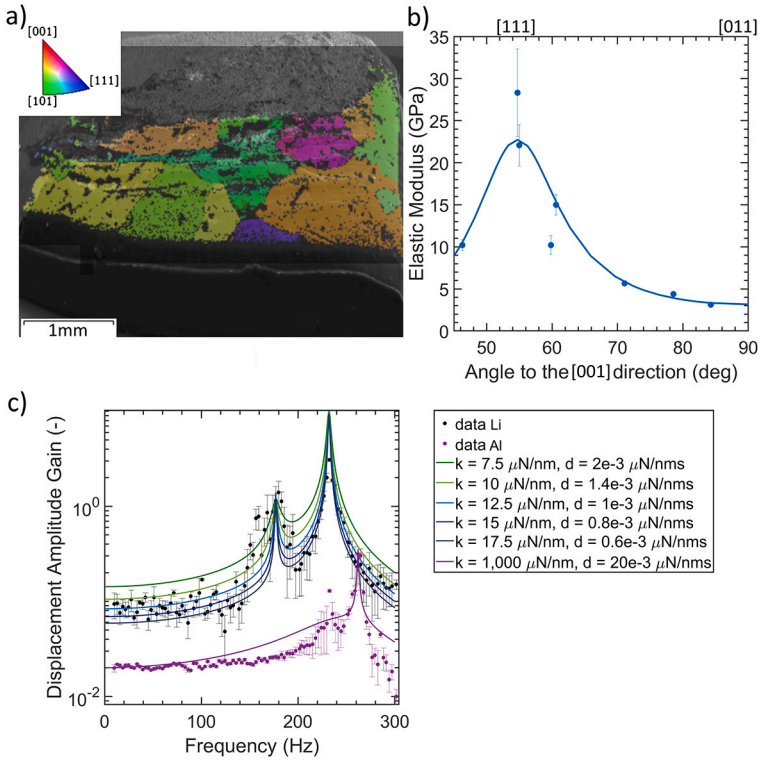

Fig. 1. a) Typical EBSD map of lithium metal with inverse pole figure colours. b) Young's Elastic Moduli vs angle with respect to the [001] with the line indicating the expected angle dependence based on the elastic constant values from Sargent and Ashby [9]. c) Frequency dependent displacement amplitude gain for a nanoDMA test at constant depth in a ⟨110⟩ grain. Errorbars denote 1 standard deviation for each point in both graphs.

3. Results and discussion

3.1. Elastic properties

Samples prepared to enable EBSD allows for nanoindentation testing of individual grains, Fig. 1a). This results in the testing of different individual orientations with respect to the [001] direction measuring the anisotropy in Young's elastic moduli, Fig. 1b). These results exhibit the expected relationship from that seen in other work with the elastic constants from Sargent and Ashby used to generate the line shown in the Fig. 1b) [9].

The visco-elastic properties are determined by the elastic modulus and coefficient of viscosity that can be related to give the time dependence of elastic displacement. This is measured with nanoindentation by applying a constant load, oscillating the tip at different frequencies and recording the displacement in a method called nanoDMA. The data from these experiments can be considered as a coupled damped harmonic oscillator as presented in [38]. Fig. 1c) shows example nanoDMA data of the measured displacement amplitude as the frequency is changed for both lithium and aluminium in black and purple, respectively. The position and magnitude of the resonant peak positions are indicative of the dominate visco-elastic properties of the material that is determined by the ratio between the stiffness and time dependent compliance of each element. The large standard deviation in the measured data is indicative that there are minor complications present in different tests that are not captured by the simple two coupled harmonic oscillators but do not affect the resonant peak position. The fits shown illustrate that the peak positions are not sensitive to the absolute stiffness but the ratio between k and d that give a relaxation time of the order of 10^{-4} s. This is 10 times larger than the effect measured on aluminium, which is assumed to have no time dependent deformation at room temperature, and fast enough to be considered instantaneous if tests are conducted below 1,000 Hz.

3.2. Plastic properties

Visco-plasticity can be considered as two different effects that lead to changes in the amount of plastic strain: the conversion of elastic strain to plastic strain (as in a Maxwell material); or the thermal removal of dislocations (annealing). A range of nanoindentation methods were conducted to consider the visco-plastic properties: constant load rate tests, constant load tests (creep), and constant displacement tests (stress relaxation). Analysis of all these test procedures is considered as the same material/model responding to different indenter methods.

For nanoindentation we propose the material is yielding when the tip depth is the greater than all times prior in the test and responding elastically when the depth is lower than the test maximum, allowing partial unload tests to be segmented for analysis as shown in Fig. 2. This figure shows example data from a stepped displacement controlled stress relaxation test where the hardness measured spikes during the increase in depth and decreases while the depth is held constant due to long-term thermal annealing. Fig. 2 illustrates this by showing an example of the gradient of the measured hardness in time during the step from one depth to the next in the displacement controlled stress relaxation test. The elastic response is shown in Fig. 2a) as a green trace with an increase until the previous maximum depth is reached and a small unloading (~ 99.25 s) related to the displacement overshoot and correction dictated by the PID settings of the instrument as shown by the tip depth vs time graph Fig. 2b). In the central region of the plot where the lithium is yielding the hardness gradient can be fitted using the combined Taylor and Orowan approach, that will be discussed further below, leaving the purple region (a large negative gradient) undescribed. In the transition from yielding to an elastic response the drop in stress is associated with the material relaxing and is at a maximum when the acceleration of the tip is most negative and decays exponentially quickly being obscured by the elastic unloading when the tip speed increases. We propose this illustrates elastic stress relaxation that can be considered as a Maxwell material under constant

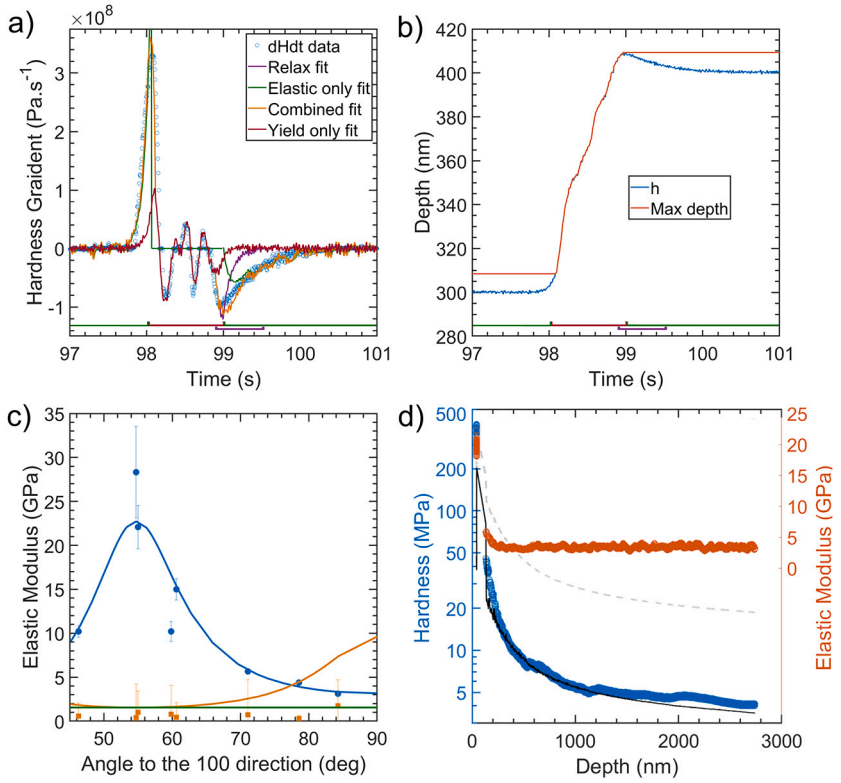

Fig. 2. a) Chronological fitting of the measured Hardness rate during a step change in depth of the indenter this illustrates the yielding, relaxing and elastic responses in time. b) Depth vs time from the same step change in depth of the indenter illustrating how the elastic and plastic responses equate to the tip position. c) Elastic Moduli (blue) from equation (6) and Shear Moduli (orange) from equation (9) vs angle with respect to the crystal 100, the lines display the expected angle dependence based on the elastic constants given by Sargent and Ashby [9]. The green line indicates the G value expected for {321}. d) Example test data from a {0.1 0 1} grain: E = 3.0±0.5 GPa mean of blue data, G = 1.9±0.3 GPa from the fit shown in black with the grey dashed line the fit with the expected G = 10 GPa.

strain (low tip speed), $\dot{H}_{elastic\,relax}$ shown in equation (7). With A as the magnitude of the stress decay the fitting gives an E/η value of 8 s^{-1} suggesting that the unimpeded dash-pot element is weaker than the spring reacting quickly (< 0.5 s) when the force is removed. Exploring this small time scale dependent change and understand the underlying mechanism is beyond the scope of this paper as it would require in-situ characterisation of the plastic deformation evolved by this rapid relaxation process. For the remainder of this study we will not consider this quick elastic stress relaxation in the model; considering that nanoindented lithium undergoes plastic deformation by strain yielding and thermal stress relaxation or just the relaxation component when the strain-rate is low enough.

$$\dot{H} = \underbrace{3\sqrt{3}(\dot{\tau_T} + \dot{\tau_O})}_{\text{yielding}} + \underbrace{E\dot{\epsilon}}_{\text{elastic}} + \underbrace{Aexp(\frac{-Et}{\eta})}_{\text{elastic relax}} \tag{7}$$

Thermal stress relaxation is present in lithium due to its low melting temperature often referred to as thermal annealing. This mechanism works over a longer time scale and is bounded by the applied stress and the athermal contribution. To capture this in all constant yield tests (linear increasing load and creep methods) the calculated stress response to the indentation is multiplied by relaxation function containing a constant athermal term and an exponentially decaying thermal term dictated by a coefficient of relaxation (K^r). This results in the full fitting equation (9) that is used to find the G value for all tests with the results shown in Fig. 2c). To fully investigate K^r splitting it into the activation volume and the thermal activation energy of this system requires a uniform stress state as provided by uni-axial loading and so is beyond the scope of the current study.

$$H = 3\sqrt{3}(\tau_T + \tau_O)(R * exp(-K^r t) + (1 - R))) \tag{8}$$

$$H = 3\sqrt{3}(\alpha Gb\sqrt{\rho_y} + \dot{\epsilon}_p B/mf_a\rho_y b^2)(R * exp(-K^r t) + (1 - R))) \tag{9}$$

$$where \qquad R = \frac{\tau_{thermal}}{\tau_{athermal}} \tag{10}$$

Using equation (9) to fit hardness data from both linear increasing load and load hold tests gives consistent results, as shown in Fig. 2c-d), but returns significantly lower shear modulus values than expected based on the orientation of indentation calculated from the Sargent and Ashby elastic coefficients [9]. Fig. 2d) shows data from a standard test with the hardness values in orange fitted with a black line associated with a shear modulus of 1.9±0.3 GPa that is considerably below the dashed line given by the expected shear modulus of 10 GPa for that orientation. Understanding this discrepancy requires considering the shear modulus that a dislocation interacts with. The dislocation motion in a yielding anisotropic material will be controlled by both the orientation of the slip systems and the direction of loading. During indentation the evolution of the stress field is complex, but the three contact faces can be considered separately and the most active slip systems in a bcc system can be calculated as given by the workings of Chen et al. [39].

This shows that for a tip indenting on a [001] face the {110} family has the highest m but the second highest (that implies the onset of stage II work hardening [40]) are a combination of {110} and {321}, Fig. 3. These results suggest the plasticity in any orientation is dominated by dislocation motion on the {321} type plane and the shear modulus data measured is orientation independent. This interpretation fits the data as shown by the green line in Fig. 2c) representing the shear modulus of the {321}.

The above calculation of yielding slip systems can be repeated for each distinct orientation of indentation and used to find the effective m and f_a to isolate the value of B for the material and best understand the Orowan strengthening, Fig. 3. An average mf_a value for each indent can be calculated using the proportion of active slip systems f_a (the number

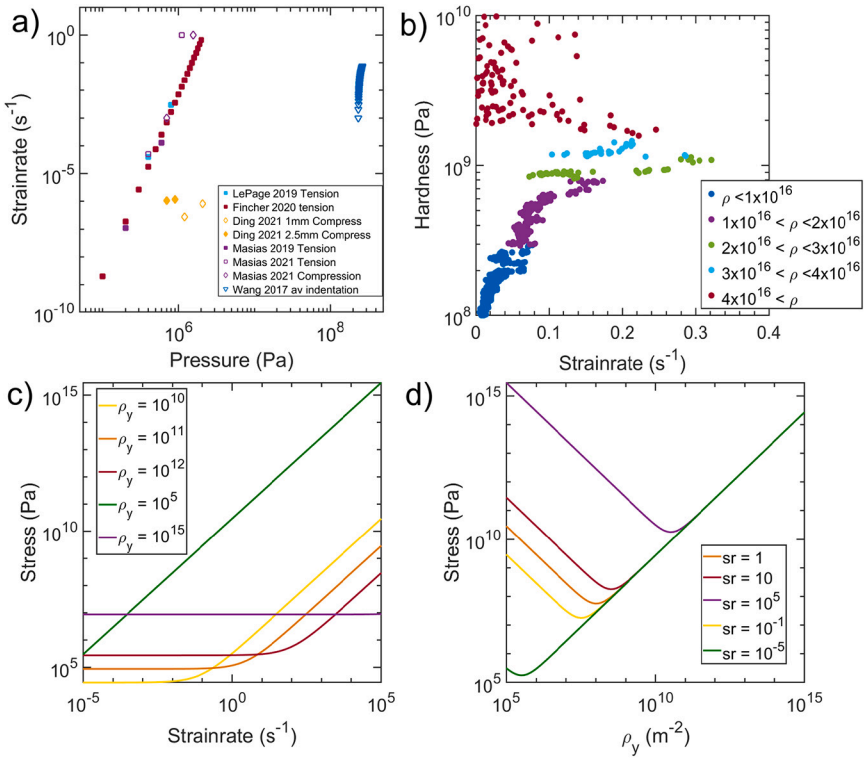

Fig. 4. a) Strain-rate vs stress for lithium tested by various methods from references [16,12–14,41], b) an example hardness data measured with increasing load plotted vs measured strain-rate ($\dot{\epsilon} = \dot{h}/h$) with colours illustrating the different dislocation densities displaying different responses, c) and d) show the results calculated using equation (11) for applied stress vs strain-rate with fixed dislocation densities and applied stress vs dislocation density with fixed strain-rates, respectively.

[001] average mfa = 0.4311			
max			
F1	$\bar{0}$	$\bar{1}$	1
F2	1	0	1
F3	1	0	1
second			
F1	0	$\bar{1}$	$\bar{1}$
F2	3	$\bar{1}$	2
F3	$\bar{3}$	$\bar{1}$	$\bar{2}$

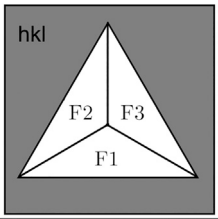

[011] average mfa = 0.4027			
max			
F1	$\bar{2}$	1	1
F2	1	0	1
F3	1	1	0
second			
F1	$\bar{3}$	1	2
F2	$\bar{3}$	$\bar{1}$	$\bar{2}$
F3	3	2	1

[111] average mfa = 0.3597			
max			
F1	3	2	1
F2	0	$\bar{1}$	$\bar{1}$
F3	2	1	3
second			
F1	$\bar{2}$	$\bar{1}$	$\bar{1}$
F2	1	3	2
F3	$\bar{1}$	$\bar{1}$	$\bar{2}$

Fig. 3. An indent schematic and the slip planes with the largest and second largest calculated Schmidt factors for each face of the indentation for each of the three major hkl crystal direction surface orientations.

of systems with $m > 0.05$ divided by the total) and the second largest m (indicating stage II hardening). Examples of these average values for mf_a for the three primary directions are shown in Fig. 3 to vary by ~ 20% and act as upper limits in the fitting process because in a real indentation test some dislocations that lie on an active slip plane could be pinned, which would reduce the f_a value.

The role of Orowan strengthening is significant when comparing the strain-rate vs pressure data from this work with that measured by others and by alternate methods, Fig. 4a). The literature values are clustered by method indicating an effect of the test conducted. Strain-rate dependence has long been considered as a function of the mobile dislocation density within a material and nanoindentation testing with its complex stress field leads to a changing dislocation structure. In tension and compression test there is a constraint of the number of dislocation sources already in the material at the start of the test. Lithium anneals easily at room temperature leading to small dislocation densities and hence lower but inconsistent reports of pressure for the same strain-rate.

The nanoindentation tests conducted here dictate a high initial strain-rate and dislocation density but fitting the data with equation (9) unpicks these effects. Fig. 4b) shows that the hardness measured is not unique for a given strain-rate and is also effected by the dislocation density. At low strain-rates the hardness measured can be different by two orders of magnetude within the same test due to the changing dislocation density. Low dislocation densities display the Orowan relationship between strain-rate and hardness with high dislocation densities dominated by Taylor hardening. The lack of unique hardness values are prevalent in the lithium literature because of the low dislocation density leading to a significant amount of Orowan type stress. Concentrating on the Orowan contribution, the minimum average B value measured for an individual grain in this study was 0.027×10^{-5} Pa.s^{-1} significantly lower than the standard value expected for a transition metal [30]. This value is not consistent across all tests as the fit combines B/mf_a meaning that in regions where the fraction of active (mobile) dislocations can have a profound effect. The maximum measured average value for B was 29.5×10^{-5} Pa.s^{-1} equating to an f_a value of 0.1% if we consider the lower value as relating to 100% of dislocations being mobile.

More generally the strain-rate can be understood as:

$$\dot{\epsilon} = \frac{mf_a\rho_y b^2}{B}(\tau_{app} - \alpha Gb\sqrt{\rho_y}) \tag{11}$$

With ρ_y dependent on test method or in the case of nanoindentation the depth at which the test is done. From Fan et al. [29] there is a minimum dislocation density which could be found by:

$$\rho_{min} = \left(\frac{2B\dot{\epsilon}}{\alpha m f_a G b^3}\right)^{\frac{2}{3}} \tag{12}$$

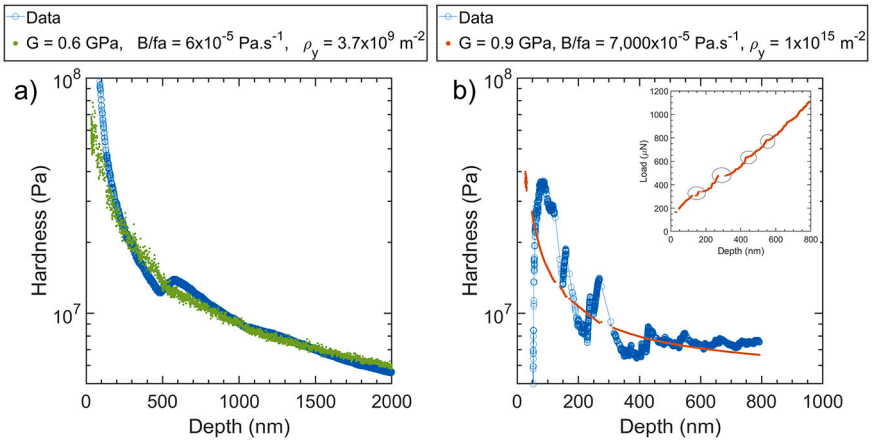

Fig. 5. Examples of discontinuities in hardness data (blue) with a fit using equation (11) (green and orange) and the fitted values: a) Low bulk dislocation density, b) low dislocation mobility, with an insert of the load displacement curve where the displacement bursts are highlighted using circles.

with a minimum applied stress of:

$$\tau_{min} = \left(\frac{27B\dot{\epsilon}G^2\alpha^2}{4mf_a}\right)^{\frac{1}{3}} \tag{13}$$

Fig. 4 c-d) show graphically equation (11)-(13) with the interrelation between stress, strain-rate, and dislocation density with the f_a value fixed at 100% and illustrates we understand the material's hardness response to any idealised nanoindentation displacement and the key nature of the dislocation density in a material where the dislocation drag coefficient is low.

This work highlights the importance of dislocation density in dictating the plastic response of the material. A unique result of small numbers of active dislocations in indentation are discontinuities (sometimes called pop-ins) that have been observed in some examples that are ill-described by equation (9) as the material is not in a constant yield condition, Fig. 5. Pop-ins are more usually observed in spherical indentation tests where there is an initial elastic loading until nucleation or unpinning of dislocations causes a jump in displacement [42]. This is seen in the lithium where the bulk dislocation density is low with a step up in hardness indicating homogeneous nucleation leading to continuous yield thereafter, Fig. 5a). In cases where the dislocation density is high but the proportion of active/mobile dislocations is low (as illustrated by a high fitted B value) successive pop-ins (stepped increase in depth) can be seen indicating activation and unlocking of pre-existing pinned dislocations, Fig. 5b). This enhanced strength when few active dislocations are present is often seen in small-scale tests and was observed in the micropillar tests of Xu et al. [11].

3.3. Thermal relaxation

Elevated temperature partial unload nanoindentation experiments allow repeat testing of the same material to consider the evolution of the microstructure and the thermal/athermal relaxation ratio. The hold segments of each partial unload were fitted using the equation (9) with good agreement, Fig. 6a). Fig. 6b) shows that tests at 25, 50, 75 and 100 °C exhibit reducing shear modulus with increasing temperature agreeing with the observations of Xu et al. [11]. The measured values for B are elevated compared with room temperature tests and with a large scatter that as discussed above is an effect of the proportion of mobile dislocations, Fig. 6c). This shows that with increasing temperature the effect of Orowan stress increases and that of Taylor stress decreases. As the partial unload nanoindentation tests proceed there is an increase in both the amount of thermal relaxation and non-recoverable athermal stress. The ratio between these two dictate how the Taylor and Orwan stresses match the observed hardness, equitation 7. Caillard suggests that elevating test temperatures makes it easier for energy barriers from localized obstacles (impurities, solute atoms and forest dislocations) to be overcome but have no effect on the absolute amount of athermal obstacles [27]. This is observed as the ratio increases from zero at an earlier time and reaching a higher peak value at higher temperatures, as shown in Fig. 6d). In a typical 25 °C test the ratio of thermal to athermal stress increases steadily with time whereas a 100 °C test increases more rapidly before plateauing at a higher value than the room temperature test, in the same period of time. The additional hardness retained at room temperature causes the depth of the test to be reduced by almost a third compared with the 100 °C test, Fig. 6e).

The strain-rate dependence of lithium is significantly effected by the dislocation structure and this recoverable and non-recoverable stress suggesting that it is crucial to consider the material's history when defining the creep properties. These findings are in agreement with the extremes illustrated in the literature by the small-scale pillars of Xu et al. [11], where the size of the volume tested reduces the absolute number of dislocations, and by the delayed tests of Masias et al. [18] where the material relaxes reducing the amount of plastic strain and mobile dislocations leading to lower strain-rates at the same pressure after different times. The dislocation density in lithium is easy to change due to the low yield stress but the retention of a chosen dislocation density for aiding cycling could be effected by the ease of stress relaxation. Further study is required to consider if the athermal defects, which are unaffected by thermal relaxation, are able to enhance the creep properties.

4. Conclusions

Nanoindentation of lithium metal in an SEM with EBSD has been used to remove the effects of surface impurities, isolate individual crystallographic orientations, and monitor the dislocation density during testing that have led to a range in mechanical properties to be reported in the literature.

This work separates the effects of crystal orientation, dislocation density and effective strainrate on lithium's mechanical properties.

Lithium responds dependent on strain and time in a way that is easiest to understand via dislocation density as discussed above. This highlights along with the elastic anisotropy why there is a range of mechanical values reported in the literature from a range of reputable sources. The reported range in elastic moduli of 4-16 GPa lies within the range we have observed for the elastic modulus dependent on crystal orientation suggesting that the 'bulk' values measured are a combination of different grain orientation responses. The 2 orders of magnitude difference in reported creep data is due to the differences in dislocation density generated by different types of experimental loading.

Recent work has suggested that lithiumcan propagate cracks in solid electrolytes via wedging open cracks [22] illustrating that the high hardness of lithium observed at small-scales by nanoindentation is important for determining stable cycling stack pressures.

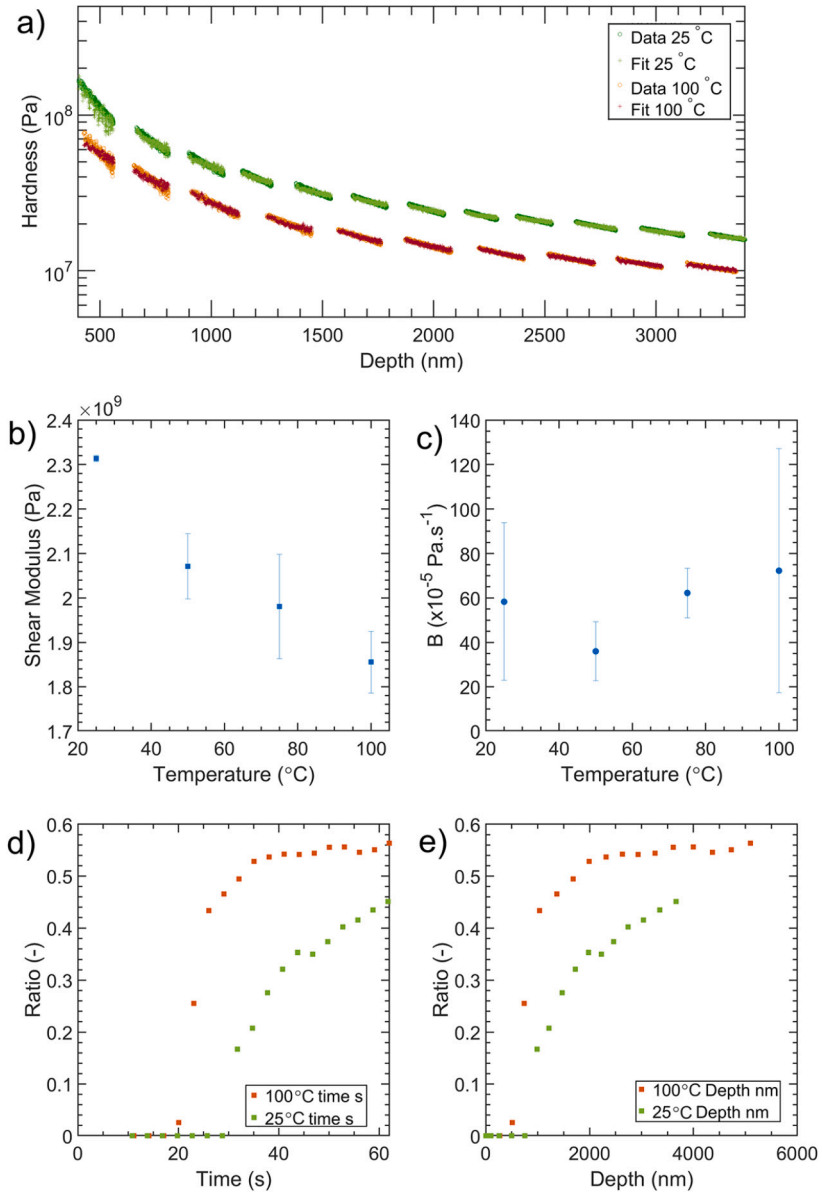

Fig. 6. a) Typical elevated temperature partial unload tests at 25 and 100 °C displaying only the load hold segments, symbol o, and their fitting with equation (11), symbol +. b-c) The relationship of shear modulus (G) and dislocation drag (B) with increasing temperature. d-e) The ratio of thermal recovery to athermal unrecoverable stress for typical tests at 25 and 100 °C with increasing test time and depth.

Given a full understanding or measurement of a samples dislocation density the minimum stress required to generate a given strain-rate can be calculated via equation (13). These results can have implications within the battery during production and cycling. The large pressure needed to form good interfaces is due to the poor wetting [3] and the large plastic work done to small volumes [43] that we have shown here only makes the material harder. The anisotropy of lithium elastic modulus means that, if paired with an argyrodite solid electrolyte [44], on the same surface neighbouring grains could have interfaces in compression or tension that would greatly effect the stripping and plating behaviour [5].

The model proposed by Monroe and Newman suggests that the solid electrolyte should be elastically stiffer than lithium to maintain interface stability and avoid dendrite growth [5]. If the anisotropy and the maximum stiffness observed in this work are not considered localised failure could occur based on the lithium crystal orientation at the interface. This suggests two potential areas for optimization: increasing the solid electrolyte stiffness or preparation of lithium anodes to select the crystallography at the interface with the electrolyte. Further developments in anode preparation could be considered to select the creep properties for cycling by picking the dislocation density that would maximise strainrate with a working stack pressure, Fig. 4 c) and d). The observation that compression produces more dislocation density than tension suggests that thin anodes could be prepared via tension and coupled with post deformation heat treatment to create anodes with low dislocation densities.

This work pulls together the disparate lithium mechanical properties data that will allow future researchers to confidently progress in linking the role of lithium's behaviour under stress with failure mechanisms in metal anode batteries.

Declaration of competing interest

The authors declare the following financial interests/personal relationships which may be considered as potential competing interests:

Ed Darnbrough reports financial support was provided by The Faraday Institution.

Data availability

The raw and processed data required to reproduce these findings cannot be shared at this time due to technical and time limitations. The data can be shared through direct contact with the corresponding author.

Acknowledgements

This work was supported by the Faraday Institution [SOLBAT FIRG026]. The authors acknowledge use of characterisation facilities within the David Cockayne Centre for Electron Microscopy, Department of Materials, University of Oxford, alongside financial support provided by the Henry Royce Institute (Grant ref EP/R010145/1).

References

[1] Lukas Porz, Tushar Swamy, Brian W. Sheldon, Daniel Rettenwander, Till Frömling, Henry L. Thaman, Stefan Berendts, Reinhard Uecker, W. Craig Carter, Yet-Ming Chiang, Mechanism of lithium metal penetration through inorganic solid electrolytes, Adv. Energy Mater. 7 (20) (oct 2017) 1701003.

[2] Mauro Pasta, David Armstrong, Zachary L. Brown, Junfu Bu, Martin R. Castell, Peiyu Chen, Alan Cocks, Serena A. Corr, Edmund J. Cussen, Ed Darnbrough, Vikram Deshpande, Christopher Doerrer, Matthew S. Dyer, Hany El-Shinawi, Norman Fleck, Patrick Grant, Georgina L. Gregory, Chris Grovenor, Laurence J. Hardwick, John T.S. Irvine, Hyeon Jeong Lee, Guanchen Li, Emanuela Liberti, Innes McClelland, Charles Monroe, Peter D. Nellist, Paul R. Shearing, Elvis Shoko, Weixin Song, Dominic Spencer Jolly, Christopher I. Thomas, Stephen J. Turrell, Mihkel Vestli, Charlotte K. Williams, Yundong Zhou, Peter G. Bruce, 2020 roadmap on solid-state batteries, J. Phys. Energy 2 (3) (aug 2020) 032008.

[3] Jeff Sakamoto, More pressure needed, Nat. Energy 4 (10) (oct 2019) 827–828.

[4] Yikai Wang, Dingying Dang, Ming Wang, Xingcheng Xiao, Yang-Tse Cheng, Mechanical behavior of electroplated mossy lithium at room temperature studied by flat punch indentation, Appl. Phys. Lett. 115 (4) (jul 2019) 043903.

[5] Charles Monroe, John Newman, The impact of elastic deformation on deposition kinetics at lithium/polymer interfaces, J. Electrochem. Soc. 152 (2) (2005) A396.

[6] Kyungho Yoon, Sunyoung Lee, Kyungbae Oh, Kisuk Kang, K. Yoon, S. Lee, K. Oh, K. Kang, Challenges and strategies towards practically feasible solid-state lithium metal batteries, Adv. Mater. 34 (4) (jan 2022) 2104666.

[7] Jean-Marie Doux, Han Nguyen, Darren H.S. Tan, Abhik Banerjee, Xuefeng Wang, Erik A. Wu, Chiho Jo, Hedi Yang, Ying Shirley Meng, J-m Doux, H. Nguyen, D.H.S. Tan, A. Banerjee, X. Wang, E.A. Wu, C. Jo, H. Yang, Y.S. Meng, Stack pressure considerations for room-temperature all-solid-state lithium metal batteries, Adv. Energy Mater. 10 (1) (jan 2020) 1903253.

[8] Hanghang Yan, Karnpiwat Tantratian, Kevin Ellwood, Elisa T. Harrison, Mark Nichols, Xiangyang Cui, Lei Chen, H. Yan, X. Cui, K. Tantratian, L. Chen, K. Ellwood, E.T. Harrison, M. Nichols, How does the creep stress regulate void formation at the lithium-solid electrolyte interface during stripping?, Adv. Energy Mater. 12 (2) (jan 2022) 2102283.

[9] P.M. Sargent, M.F. Ashby, Deformation mechanism maps for alkali metals, Scr. Metall. 18 (2) (feb 1984) 145–150.

[10] T. Slotwinski, J. Trivisonno, Temperature dependence of the elastic constants of single crystal lithium, J. Phys. Chem. Solids 30 (5) (may 1969) 1276–1278.

[11] Chen Xu, Zeeshan Ahmad, Asghar Aryanfar, Venkatasubramanian Viswanathan, Julia R. Greer, Enhanced strength and temperature dependence of mechanical properties of Li at small scales and its implications for Li metal anodes, Proc. Natl. Acad. Sci. 114 (1) (jan 2017) 57–61.

[12] Cole D. Fincher, Daniela Ojeda, Yuwei Zhang, George M. Pharr, Matt Pharr, Mechanical properties of metallic lithium: from nano to bulk scales, Acta Mater. 186 (mar 2020) 215–222.

[13] Alvaro Masias, Nando Felten, Regina Garcia-Mendez, Jeff Wolfenstine, Jeff Sakamoto, Elastic, plastic, and creep mechanical properties of lithium metal, J. Mater. Sci. 54 (2019) 2585–2600.

[14] Yikai Wang, Yang Tse Cheng, A nanoindentation study of the viscoplastic behavior of pure lithium, Scr. Mater. 130 (mar 2017) 191–195.

[15] Tobias Sedlatschek, Junhe Lian, Wei Li, Menglei Jiang, Tomasz Wierzbicki, Martin Z. Bazant, Juner Zhu, Large-deformation plasticity and fracture behavior of pure lithium under various stress states, Acta Mater. 208 (apr 2021) 116730.

[16] William S. LePage, Yuxin Chen, Eric Kazyak, Kuan-Hung Chen, Adrian J. Sanchez, Andrea Poli, Ellen M. Arruda, M.D. Thouless, Neil P. Dasgupta, Lithium mechanics: roles of strain rate and temperature and implications for lithium metal batteries, J. Electrochem. Soc. 166 (2) (2019) A89–A97.

[17] Lallit Anand, Sooraj Narayan, An elastic-viscoplastic model for lithium, J. Electrochem. Soc. 166 (6) (apr 2019) A1092–A1095.

[18] Alvaro Masias, Nando Felten, Jeff Sakamoto, Characterizing the mechanical behavior of lithium in compression, J. Mater. Res. 36 (3) (jan 2021) 729–739.

[19] Rishi Raj, Stack pressure and critical current density in Li-metal cells: the role of mechanical deformation, Acta Mater. 215 (aug 2021) 117076.

[20] Qiongjie Ke, Qingshuai Xu, Xuejun Lai, Xianfeng Yang, Huichun Gao, Zaisheng Wang, Yongcai Qiu, Ultralong-life lithium metal batteries enabled by decorating robust hybrid interphases on 3D layered framworks, Chin. Chem. Lett. 34 (5) (may 2023) 107602.

[21] Jiang Kui Hu, Hong Yuan Shi Jie Yang, Yang Lu, Shuo Sun, Jia Liu, Yu Long Liao, Shuai Li, Chen Zi Zhao, Jia Qi Huang, Dry electrode technology for scalable and flexible high-energy sulfur cathodes in all-solid-state lithium-sulfur batteries, J. Energy Chem. 71 (aug 2022) 612–618.

[22] Ziyang Ning, Guanchen Li, Dominic L.R. Melvin, Yang Chen, Junfu Bu, Dominic Spencer-Jolly, Junliang Liu, Bingkun Hu, Xiangwen Gao, Johann Perera, Chen Gong, Shengda D. Pu, Shengming Zhang, Boyang Liu, Gareth O. Hartley, Andrew J. Bodey, Richard I. Todd, Patrick S. Grant, David E.J. Armstrong, T. James Marrow, Charles W. Monroe, Peter G. Bruce, Dendrite initiation and propagation in lithium metal solid-state batteries, Nature 618 (7964) (jun 2023) 287–293.

[23] Xin Lei Gao, Wen Long Xie Hua Liu, Xin Li Sheng Zhang, Multiscale observation of Li plating for lithium-ion batteries, Rare Met. 40 (11) (nov 2021) 3038–3048.

[24] Anthony Ferrese, John Newman, Mechanical deformation of a lithium-metal anode due to a very stiff separator, J. Electrochem. Soc. 161 (9) (2014) A1350–A1359.

[25] Erik G. Herbert, Stephen A. Hackney, Violet Thole, Nancy J. Dudney, P. Sudharshan Phani, Nanoindentation of high-purity vapor deposited lithium films: a mechanistic rationalization of diffusion-mediated flow, 2019.

[26] Yang Tse Cheng, Che Min Cheng, Scaling, dimensional analysis, and indentation measurements, aug 2004.

[27] Daniel Caillard, Jean-Luc Martin, Thermally activated mechanisms in crystal plasticity, 2003, p. 433.

[28] S. Tariq, K. Ammigan, P. Hurh, R. Schultz, P. Liu, J. Shang, Li material testing-Fermilab antiproton source lithium collection lens, in: Proc. IEEE Part. Accel. Conf., vol. 3, 2003, pp. 1452–1454.

[29] Haidong Fan, Qingyuan Wang, Jaafar A. El-Awady, Dierk Raabe, Michael Zaiser, Strain rate dependency of dislocation plasticity, Nat. Commun. 12 (1) (mar 2021) 1–11.

[30] David L. Olmsted, Louis G. Hector, W.A. Curtin, R.J. Clifton, Atomistic simulations of dislocation mobility in Al, Ni and Al/Mg alloys, Model. Simul. Mater. Sci. Eng. 13 (2005) 371–388.

[31] William D. Nix, Huajian Gao, Indentation size effects in crystalline materials: a law for strain gradient plasticity, J. Mech. Phys. Solids 46 (3) (mar 1998) 411–425.

[32] A. Leitner, V. Maier-Kiener, D. Kiener, Dynamic nanoindentation testing: is there an influence on a material's hardness?, http://mc.manuscriptcentral.com/tmrl 5 (7) (nov 2017) 486–493.

[33] Jack Aspinall, David E.J. Armstrong, Mauro Pasta, EBSD-coupled indentation: nanoscale mechanics of lithium metal, Mater. Today Energy 30 (2022) 101183.

[34] Liqiang Zhang, Tingting Yang, Congcong Du, Qiunan Liu, Yushu Tang, Jun Zhao, Baolin Wang, Tianwu Chen, Yong Sun, Peng Jia, Hui Li, Lin Geng, Jingzhao Chen, Hongjun Ye, Zaifa Wang, Yanshuai Li, Haiming Sun, Xiaomei Li, Qiushi Dai, Yongfu Tang, Qiuming Peng, Tongde Shen, Sulin Zhang, Ting Zhu, Jianyu Huang, Lithium whisker growth and stress generation in an in situ atomic force microscope–environmental transmission electron microscope set-up, Nat. Nanotechnol. 15 (2) (jan 2020) 94–98.

[35] Alexander Yulaev, Vladimir Oleshko, Paul Haney, Jialin Liu, Yue Qi, A. Alec Talin, Marina S. Leite, Andrei Kolmakov, From microparticles to nanowires and back: radical transformations in plated Li metal morphology revealed via in situ scanning electron microscopy, Nano Lett. 18 (3) (mar 2018) 1644–1650.

[36] W.C. Oliver, G.M. Pharr, An improved technique for determining hardness and elastic modulus using load and displacement sensing indentation experiments, J. Mater. Res. 7 (6) (jan 2011) 1564–1583.

[37] J.B. Pethica, W.C. Oliver, Mechanical properties of nanometre volumes of material: use of the elastic response of small area indentations, MRS Online Proc. Libr. 130 (1) (dec 1988) 13–23.

[38] E. Darnbrough, Interpretation of dynamic nanoindentation results a simple harmonic oscillators for measurement of viscoelasticity, arXiv, 2022.

[39] Siwei Chen, Yuichi Miyahara, Akiyoshi Nomoto, Crystallographic orientation dependence of nanoindentation hardness in austenitic phase of stainless steel 98 (11) (nov 2019) 473–485, https://doi.org/10.1080/09500839.2019.1577997.

[40] T.E. Mitchell, R.A. Foxall, P.B. Hirsch, Work-hardening in niobium single crystals 8 (95) (2006) 1895–1920, https://doi.org/10.1080/14786436308209081.

[41] Shaochen Ding, Logan Fairgrieve-Park, Oles Sendetskyi, Michael D. Fleischauer, Compressive creep deformation of lithium foil at varied cell conditions, J. Power Sources 488 (mar 2021) 229404.

[42] Fabian Pöhl, Pop-in behavior and elastic-to-plastic transition of polycrystalline pure iron during sharp nanoindentation, Sci. Rep. 9 (1) (oct 2019) 1–12.

[43] Xin Zhang, Q. Jane Wang, Katharine L. Harrison, Scott A. Roberts, Stephen J. Harris, Pressure-driven interface evolution in solid-state lithium metal batteries, Cell Reports Phys. Sci. 1 (2) (feb 2020) 100012.

[44] Xiangtao Bai, Yi Duan, Weidong Zhuang, Rong Yang, Jiantao Wang, Research progress in Li-argyrodite-based solid-state electrolytes, J. Mater. Chem. A 8 (48) (dec 2020) 25663–25686.